

Finite element modeling of laser ultrasonics nondestructive evaluation technique in ablation regime

Salman Shamsaei and Farhang Honarvar*

*NDE Lab, Faculty of Mechanical Engineering, K. N. Toosi University of Technology,
7 Pardis St., Mollasadra Ave., Vanak Sq., Tehran, Iran*

(Received August 31, 2022, Revised May 9, 2023, Accepted May 10, 2023)

Abstract. In this paper, finite element modeling of the laser ultrasonics (LU) process in ablation regime is of interest. The momentum resulting from the removal of material from the specimen surface by the laser beam radiation in ablation regime is modeled as a pressure pulse. To model this pressure pulse, two equations are required: one for the spatial distribution and one for the temporal distribution of the pulse. Previous researchers have proposed various equations for the spatial and temporal distributions of the pressure pulse in different laser applications. All available equations are examined and the best combination of the temporal and spatial distributions of the pressure pulse that provides the most accurate results is identified. This combination of temporal and spatial distributions has never been used for modeling laser ultrasonics before. Then by using this new model, the effects of variations in pulse duration and laser spot radius on the shape, amplitude, and frequency spectrum of ultrasonic waves are studied. Furthermore, the LU in thermoelastic regime is simulated by this model and compared with LU in ablation regime. The interaction of ultrasonic waves with a defect is also investigated in the LU process in ablation regime. Good agreement of the results obtained from the new finite element model and available experimental data confirms the accuracy of the proposed model.

Keywords: ablation regime; finite element modeling; laser ultrasonics; nondestructive evaluation; pressure pulse

1. Introduction

In nondestructive evaluation (NDE), laser ultrasonics (LU) can be used in two regimes: thermoelastic or ablation. In the thermoelastic regime, the laser energy is low and as the laser pulse hits the surface, the instantaneous thermal expansion of the material leads to the formation of an ultrasonic wave. If the density of the laser energy is increased, as the laser hits the surface, in addition to thermal expansion of the surface, the material also starts to evaporate. This evaporation and subsequent dissipation of matter creates a momentum that leads to the formation of ultrasonic waves in the specimen. This is called ablation regime. When examining high temperature surfaces, thick specimens, or porous materials, there is a high level of wave attenuation, making ultrasonic waves with higher energy preferable. Additionally, the ablation regime is more efficient than the thermoelastic regime in applications where partial erosion of the surface is acceptable due to the higher signal-to-noise ratio (SNR) available in the ablation regime.

*Corresponding author, Professor, E-mail: honarvar@kntu.ac.ir

Works dealing with laser ultrasound date back to 1960s and reach their peak in early 1980s (Davies *et al.* 1993). After this time, the research activities are mostly concerned with thermoelastic regime due to its nondestructive character. Fassbender *et al.* (1989) investigated the effect of laser energy density on the amplitude of longitudinal and transverse waves in the ablation regime by experimental studies. Murray and Wanger (1998) modeled laser ultrasound in the ablation regime and compared it with experiments. Their model was in good agreement with their experiments at low laser energy densities; but at higher energies, their results did not show match well with experiments due to plasma formation. Hopko and Ume (1999) conducted experimental studies on the directivity pattern of longitudinal and transverse waves generated by laser ultrasound in thermoelastic and ablation regimes. Mi and Ume (2002) investigated the effect of laser energy density, thickness and material type on the frequency bandwidth and center frequency of ultrasonic waves in the ablation regime. Stratoudaki *et al.* (2003) investigated carbon dioxide, neodymium-doped yttrium aluminum garnet (Nd:YAG), and excimer lasers in the production of ultrasonic waves in epoxy resin and the effect of the wavelength of these three lasers on the amplitude of waves produced in epoxy resin in carbon fiber-reinforced composites in both thermoelastic and ablation regimes. Pan *et al.* (2004) proposed a model for measuring the elastic constants of a specimen in both thermoelastic and ablation regimes and compared their results with experiments. Arrigoni *et al.* (2008) studied the tensile stresses due to ablation on adhesive joints by using both finite element modeling and experiments. Dai *et al.* (2010) used finite element method to model the detection of surface notches with different depths and orientations by laser ultrasound. They could find the location of the notches by Rayleigh waves and utilized shear waves to determine the depth and orientation of the notches. Pan *et al.* (2010) proposed a physical model for predicting the propagation of ultrasonic waves from a linear laser pulse in a two-layer cylinder in the ablation regime and compared the wave arrival times, shapes and amplitudes of the longitudinal and transverse waves. Sakamoto *et al.* (2011) measured the directivity of longitudinal waves in aluminum specimens in the ablation regime for a laser point-source and compared the laboratory results with theory. Using the shadow method, Pei *et al.* (2012) developed a numerical model based on the finite element method for crack detection in thermo-elastic regime and compared their results with experiments. Guo *et al.* (2014) numerically modeled the effect of an oblique force source on the energy distribution of surface and bulk waves in the ablation regime. Zhou *et al.* (2015) investigated the detection of surface-breaking cracks through finite element modeling of laser ultrasonics. They analyzed the interaction of Rayleigh waves with cracks in the time and frequency domain and compared their numerical results with experimental data. Yang *et al.* (2015) proposed an impedance measurement system using laser ultrasonics to identify pipe corrosion and screw loosening. Sherman *et al.* (2015) numerically calculated the stresses of surface waves generated by laser ablation at the interface of the coating material that covered a fused silica plate. They also compared their numerical results with experiments. Taheri *et al.* (2017) used laser ultrasound for nondestructive testing of additive manufacturing components made from SS17 4 PH stainless steel in both thermoelastic and ablation regimes. By using the finite element method, they modeled the laser ultrasonics in the cooling phase of the additive manufacturing process. Abbas and Lee (2018) used a high-speed angular ultrasonic system to detect defects in aluminum and carbon fiber-reinforced polymer (CFRP) honeycomb sandwich structures and showed that their proposed system performed well in visualizing defects. Choi and Jhang (2018) conducted numerical and experimental studies on the detection of internal defects by using longitudinal waves formed in the ablation regime. Lee *et al.* (2019) used a numerical model to investigate the effect of ablation on the shape of elastic waves that were generated by a laser

pulse and compared their numerical results with experiments by using least squares method. Liu *et al.* (2020) identified the location of fatigue cracks by ultrasonic nonlinear modulation of narrowband ultrasound waves. They carried out their experiments on aluminum sheets with real fatigue cracks. Ma *et al.* (2020) used laser opto-ultrasonic dual method for real-time detection of structural imperfections and measurement of residual stress in aluminum alloy components made by arc+wire additive manufacturing process. A Q-switched Nd: YAG laser with a wavelength of 532 nm and a pulse width of 8 ns was utilized as the source of ablation. By emitting a 60-mJ laser beam on the surface, ultrasonic waves were generated inside the component. The residual stress distribution and presence of structural defects were extracted from the optical spectra. They also compared their results with traditional methods and verified the accuracy and reliability of their method.

In this paper, laser ultrasonics is modeled in ablation regime by 2D finite element method and the effects of laser parameters on the resulting ultrasonic waves are studied. Various equations have already been proposed in different laser applications for simulating the pressure pulse that results from the momentum generated by material ablation. Some of these equations give the spatial distribution and some give the temporal distribution of the pressure pulse. Our objective is to find the best combination of spatial and temporal equations for simulating laser ultrasonics in ablation regime. All available spatial and temporal distribution equations are examined, and the best combination of these equations is identified. This combination is then used for simulating LU in ablation regime and the results are compared with experimental data available in the literature. The effects of laser spot diameter and pulse length on the amplitude, shape and frequency of the resulting ultrasonic waves are also investigated. The results obtained for the ablation regime are also compared with the results obtained for thermoelastic regime.

2. Ultrasound generation in the ablation regime

In the ablation regime of laser ultrasonic testing, ultrasonic waves are mainly generated by the momentum created from the removal of material by the impact of laser pulses on the surface. However, the actual removal of material from the surface is negligible. Moreover, the contribution of thermoelastic effects in the generation of ultrasonic waves can also be disregarded in the ablation regime. As a result, the calculations do not take into account the effects of material removal and thermoelastic deformations. The elastodynamic equation of the wave generated in the ablation regime is (Sherman *et al.* 2015):

$$\rho \frac{\partial^2 u_i(\mathbf{x}; t)}{\partial t^2} = \frac{\partial \sigma_{ij}(\mathbf{x}; t)}{\partial x_j} \quad (1)$$

where ρ is the density, u_i is the displacement component of the particle in direction i , and σ_{ij} are the components of the stress tensor. The material is isotropic and follows linear elasticity. Removal of matter creates a reaction force that causes a momentum change on the surface. The reaction force that leads to the generation of the ultrasonic waves can be applied as a boundary force (F_A) according to the following equation (Choi and Jhang 2018):

$$\sigma \cdot n = F_A \quad (2)$$

where n is the normal vector on the boundary. The boundary force can be expressed as (Wang *et al.* 2016):

Table 1 Equations for the temporal distribution of pressure pulses as used in the literature

Reference	Equation	Eq. Number
Choi and Jhang 2018	$g(t) = \exp\left(-2.7726 \frac{(t-\tau)^2}{\tau^2}\right)$	(6)
Kim <i>et al.</i> 2013	$g(t) = \begin{cases} \left \frac{t}{\tau}\right & 0 < t < \tau \\ 2 - \left \frac{t}{\tau}\right & \tau < t < 2\tau \end{cases}$	(7)
Halilovic <i>et al.</i> 2016	$g(t) = \begin{cases} 1 & 0 < t < \tau \\ \left[1 + (1+\gamma)\left(\frac{t}{\tau} - 1\right)\right]^{-\frac{\gamma}{1+\gamma}} & t > \tau \end{cases}$	(8)
Sherman <i>et al.</i> 2015	$g(t) = \frac{t^3}{\tau^4} \exp\left(\frac{-2t^2}{\tau^2}\right)$	(9)
Wang <i>et al.</i> 2016	$g(t) = \begin{cases} (k\tau)^{-2} (2k\tau - t)t & 0 \leq t \leq k\tau \\ \exp\left(\ln 0.5 \sqrt{\frac{\frac{t}{\tau} - k}{\eta - \frac{k}{\sqrt{2}}}}\right) & k\tau \leq t \leq m\tau \end{cases}$	(10)

$$F_A(x, t) = P_{max} f(x) g(t) \quad (3)$$

where $f(x)$ and $g(t)$ are the spatial and temporal distribution functions of the pressure pulse, respectively, and P_{max} is the peak value of the pressure pulse that is estimated by (Ecault *et al.* 2016):

$$P_{max} = \sqrt{I} \quad (4)$$

and I is the laser energy density expressed as (Cavuto *et al.* 2015):

$$I = E(1 - R)/\tau A \quad (5)$$

In Eq. (5), E is the energy, R is the reflection coefficient, τ is the pulse duration and A is the area of the laser spot. Different equations have been proposed for $f(x)$ and $g(t)$ in both laser ultrasonics and laser shock peening applications. The $g(t)$ equations used by previous researchers are listed in Table 1. In laser ultrasonics, Eq. (6) has been proposed for temporal distribution in (Choi and Jhang 2018), where t is the time and τ is the laser pulse duration. In (Kim *et al.* 2013), Eq. (7) is used for modeling of laser shock peening, and (Halilovic *et al.* 2016) suggests Eq. (8) for $g(t)$ in laser shock peening applications, where γ is the plasma adiabatic coefficient and is typically taken between 1.01 to 2.0 (Avillez *et al.* 2018, Martynenko *et al.* 2019). The equation used in (Sherman *et al.* 2015) for $g(t)$ in laser ultrasonics is according to Eq. (9). Reference (Wang *et al.* 2016) uses the (10) for the temporal distribution of the pressure pulse in laser shock peening process, where k, η and m are the fitting parameters of pressure pulse relative to the laser pulse. The η factor multiplies the duration of the pressure pulse, and its

Table 2 Spatial distribution equations of pressure pulse as used in the literature

Reference	Equation	Eq. Number
Choi and Jhang 2018	$f(x) = \exp\left(-2\left(\frac{x}{x_0}\right)^2\right)$	(11)
Hfaiedh <i>et al.</i> 2015, Zhao <i>et al.</i> 2017	$f(x) = \sqrt{1 - \frac{x^2}{2x_0^2}}$	(12)
Wang <i>et al.</i> 2016, Halilovic <i>et al.</i> 2016	$f(x) = \exp\left(\frac{-x^2}{2x_0^2}\right)$	(13)
Sherman <i>et al.</i> 2015, Guo <i>et al.</i> 2014	$f(x) = \exp\left(\frac{-x^2}{x_0^2}\right)$	(14)

typical value is taken approximately between 2 to 3. Eqs. (6)-(7) and (9) are appropriate for the range of laser energy being considered, but when higher laser energy densities are needed for inspection, the resulting momentum becomes significant, and the pressure pulse predicted by these equations deviates from experimental results. Eq. (10), which is commonly used in laser shock peening processes, is better suited for stronger pressure pulses. By adjusting the parameters k , η , and m , the rise time and duration of the pressure pulse can be modified, and the model can be brought into agreement with laboratory tests. Additionally, in Eq. (8), the time distribution profile of the pressure pulse can be adjusted for various energy densities by altering the plasma adiabatic coefficient (γ).

Different equations are also proposed for spatial distribution of the pressure pulse. Like the equations of temporal distribution, the equations of spatial distribution are also proposed in numerical modeling of either laser ultrasonics or laser shock peening. Conformity of these equations with the experimental results which are reported in (Sakamoto *et al.* 2011) will be considered in section 4. The $f(x)$ equations used by previous researchers are listed in Table 2.

Reference (Choi and Jhang 2018) deals with laser ultrasonics and suggests Eq. (11) for $f(x)$, where x is the distance and x_0 is the laser spot radius. In (Hfaiedh *et al.* 2015) and (Zhao *et al.* 2017), where laser shock peening is of interest, $f(x)$ corresponds to Eq. (12). Some references have used Eq. (13) for modeling the laser shock peening process (Wang *et al.* 2016, Halilovic *et al.* 2016). References (Sherman *et al.* 2015) and (Guo *et al.* 2014) suggest Eq. (14) for $f(x)$ in laser ultrasonics applications. Eqs. (11)-(14) are not much different from each other and their corresponding spatial distributions will be discussed in Section 4. In the next Section, we will examine each of the above equations to see which combination of spatial and temporal equations are more suitable for modeling a pressure pulse in laser ultrasonics in ablation regime.

3. Numerical simulation

In this section, laser ultrasonics in ablation regime is modeled in two dimensions by finite element method using Salome-Mecca software package (Code-Aster User Manual, 2017). Salome-Mecca is an integrated open-source software package that uses Salome platform for preprocessing and post-processing operations and Code-Aster for finite element analysis. In the first part of the

Table 3 Physical properties of Al6061-t6 aluminum alloy (Deiterding *et al.* 2007, Rao *et al.* 2014)

Value	Unit	Variable
69	GPa	Young's modules
0.33	-	Poisson's ratio
2719	kg/m ³	Density
163	W/m °C	Thermal conductivity
896	J/kg °C	Specific heat
652	°C	Melting point

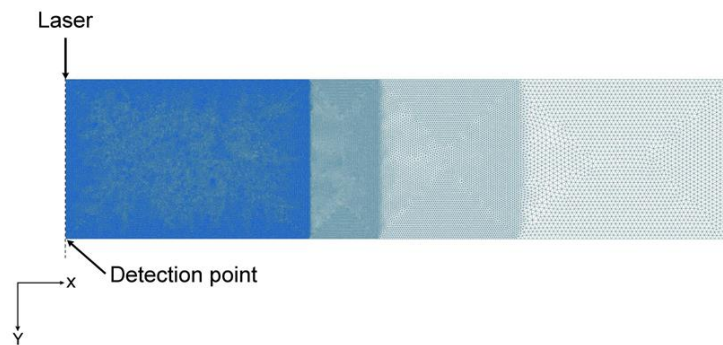


Fig. 1 Geometry and meshing of the model

simulations (Sections 4.1 and 4.2), calculations are done for a sample of Al6061-t6 aluminum alloy using a laser with a 0.15-mm spot radius and 17-ns pulse duration. The physical properties of Al6061-t6 aluminum alloy are given in Table 3.

The computational time required for complex processes such as laser ultrasonics is significant, and solving the problem in three dimensions can result in an high increase in the computation time and cost. The simulations are performed in 2D and the sample size is 38.4×4.6 mm. Due to the symmetry of the problem along the vertical axis, only half of the specimen needs to be modeled. In the finite element model, the sizes of the elements play a determinative role in computation time; therefore, the choice of the optimal mesh is of particular importance. If the element size is too small, the computation time escalates and if it is too large, the accuracy declines. The maximum element size should be chosen such that the smallest wavelength would cover at least 10 nodes (Wang *et al.* 2007). By using the longitudinal wave velocity and the radius of the laser spot, the maximum element size can be found from the following equation (Zhao *et al.* 2007):

$$L_e \leq \frac{1}{10} \frac{C}{f_{\max}} \quad (15)$$

where L_e is the maximum element size, C is the wave velocity, and f_{\max} is the highest frequency of ultrasonic waves, $f_{\max} = 5$ MHz. An element size of 0.015 mm was used for the first four microseconds of the laser impulse. To reduce the computation time after the first four microseconds, larger element sizes were gradually introduced into the model afterwards. The geometry and meshing of the model are shown in Fig. 1.

Another important factor affecting the computation time is the time step. The time step is directly related to the mesh size, and if not optimized, it can significantly increase the computation

time. The following equation provides a good estimate of the time step (Wang *et al.* 2007):

$$\Delta t \leq \frac{L_e}{C\sqrt{3}} \quad (16)$$

By using the element size obtained from Eq. (15), the maximum time step is found to be equal to 2 ns.

4. Results and discussion

4.1 Intact sample

Laser ultrasonics in the ablation regime (normal force source) is modeled in 2D by finite element method using Code-Aster solver on an Al6061-t6 aluminum alloy specimen. In all calculations, the laser energy density is kept constant and the effects of laser parameters on the shape, amplitude, and frequency of the ultrasonic waves are examined. A laser with a pulse duration of 17 ns and a spot radius of 0.15 mm is used for generating the ultrasonic waves. Different researchers have used different equations for modeling the spatial and temporal distribution of the pressure pulse that is generated by laser ablation. Some of these equations will be examined here to see which one is more consistent with experimental results reported for laser ultrasonics applications in ablation regime.

A laser pulse with an energy density of 78 J/cm² is irradiated on the top surface of the specimen and the surface displacement is measured at a point on the bottom surface. For this situation, we first consider each of the Eqs. (6)-(10) for the temporal distribution of the pressure pulse in modeling the problem. The results are plotted in Fig. 2 along with the experimental results reported by Sakamoto *et al.* (2011). In (Sakamoto *et al.* 2011) a 1064 nm Nd: YAG laser with a pulse width of 17 ns, pulse energy of 55 mJ and spot radius of 0.15 mm is used to generate ultrasonic waves, and a Mach-Zehnder type optical interferometer with a frequency range of 50 kHz to 20 MHz is used to detect the ultrasound waves. Fig. 2 shows the time-displacement curve for a node at the bottom of the sample and along the centerline of the laser beam with a pulse duration of 17 ns and a spot radius of 0.15 mm. In Fig. 2, we see that the results obtained from incorporating Eqs. (8) and (10) are more consistent with experimental results. The plasma adiabatic coefficient (γ) of Eq. (8) is 1.2, and the pulse fitting parameters of Eq. (10) for $k = 2$, $\eta = 4$ and $m = 100$ result in a curve that is well consistent with experimental results. To calculate the coefficient m in Eq. (10), a relation is proposed in reference (Wang *et al.* 2016). Due to the uncertainty of how to calculate the error parameter in this relation, it was not used in the calculations. Theoretical extraction of temporal changes of pressure pulse as a function of laser and specimen material parameters is a difficult physical problem. Therefore, a more accurate pressure-time history is obtained from laboratory observations (Achintha and Nowell 2011). Eqs. (8) and (10) can be used for various laser energy densities in ablation regime (normal force source). By changing the plasma adiabatic coefficient and the pressure pulse parameters, the temporal distribution of the pressure pulse can be adjusted to the measured data. In Eq. (8), the plasma adiabatic coefficient is varied between 1.01 and 2 to match the modeled curve to experiments. It is worth noting that Eqs. (8) and (10) have been initially used for modeling the laser shock peening process and have not been considered for modeling laser ultrasonics yet. Therefore, it seems that the equations used for modeling the laser shock peening process, can provide better results in the case of laser ultrasonics.

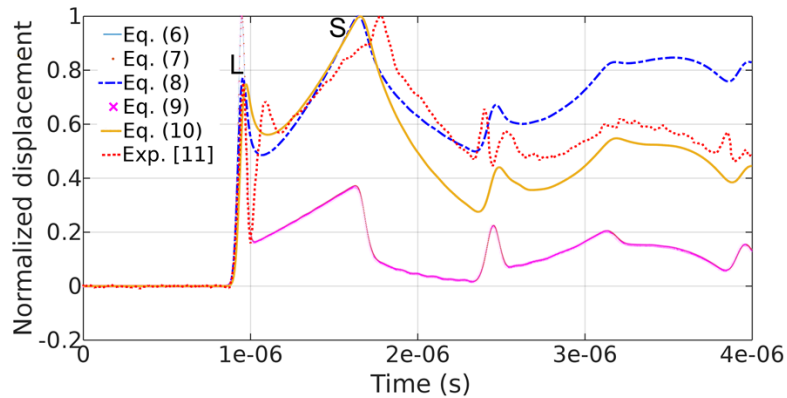


Fig. 2 Time-displacement curves of a node on the bottom surface of the specimen along the laser centerline plotted by using Eqs. (6)-(10) for modeling of the pressure pulse. Experimental results of (Sakamoto *et al.* 2011) are also included. The laser has a pulse duration of 17 ns and a spot radius of 0.15 mm

The first peak (designated by L in Fig. 2) is due to the arrival time of the longitudinal wave (L) and the second peak (designated by S) depicts the arrival time of the shear wave. A time shift is observed in the finite element model with respect to the experimental results reported in (Sakamoto *et al.* 2011). In numerical simulations, the time is measured from the moment the laser pulse strikes the top surface of the specimen. However, in laboratory tests, the origin of time can be the ignition of the xenon flash lamp and the Q-switched trigger pulse. Depending on the amount of pumped energy, the opening time of the Q-switch and laser firing instance may change. In finite element simulations, if the origin is shifted by 178 nanoseconds, the numerical results match with the experimental signal (Fig. 2). In Fig. 2, the longitudinal wave (L) resulting from Eq. (8) almost matches the experimental results; however, the shear wave (S) arrival time is slightly earlier when compared with its experimental counterpart. This time shift can be attributed to the melting of a small part of the surface material in the ablation regime which subsequently evaporates. The transverse wave does not form within the molten pool and only appears beyond this area. Since this phase change process is not considered in the numerical model, the transverse wave arrival time in the finite element model is a bit earlier than the experiment. In addition, variations of the Poisson's ratio due to the increase of temperature leads to a decrease in wave velocity (Gondrad *et al.* 1998). Therefore, all aforementioned factors, which include difference in time origin, not accounting for phase-change process, assumption of temperature-independent material properties, and possible difference in material properties in simulations and experiment, contribute to the minor differences in numerical and experimental results.

As discussed in Section 2, different equations are available for spatial distribution of the laser pulse. The spatial distribution of the pressure pulse with a spot radius of 0.15 mm is plotted in Fig. 3 by using Eqs. (11)-(14).

Time-displacement curves for a node on the bottom surface of the specimen along the laser centerline are plotted by using Eqs. (11)-(14) in Fig. 4a. In Fig. 4a, no noticeable changes are observed in the shape of the curves and only the amplitudes of the curves are different. The frequency spectra of the curves shown in Fig. 4a are plotted in Fig. 4b. In calculating the frequency spectra of these curves and those that will be presented later, the DC component of the signal is removed.

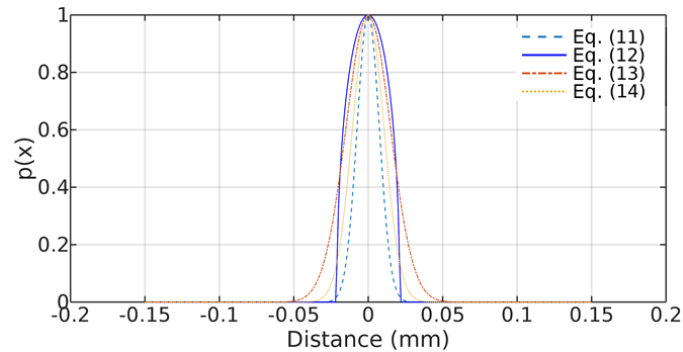


Fig. 3 Spatial distribution of laser pulse on the top surface of the specimen plotted by using Eqs. (11) to (14)

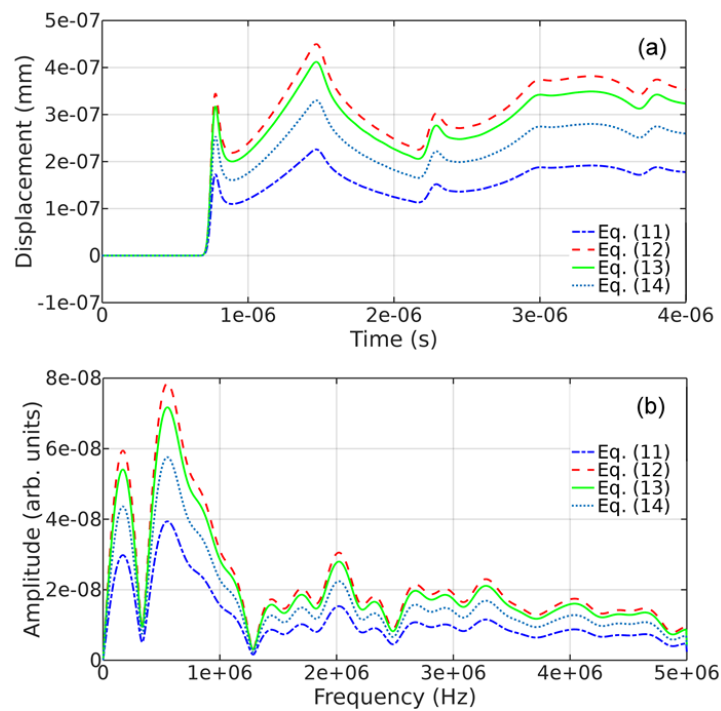


Fig. 4 Simulated ultrasonic waves received at a node on the bottom surface of the specimen. The calculations are performed by incorporating Eqs. (11)-(14) for spatial distribution of the laser pulse on the top surface of the specimen; a) time-domain signals, and b) frequency spectra

No significant changes were observed in the shape of the ultrasonic waves by using any of the four Eqs. (11)-(14) that have already been used for spatial distribution. Therefore, the main factor affecting the formation of ultrasonic waves within the part is the temporal distribution of the pressure pulse. Among the five different equations that have already been used for temporal distribution of the laser pressure pulse, Eqs. (8) and (10) were able to provide results that are more consistent with experiments. Between these two equations, we will be using Eq. (8) for the temporal distribution of the pressure pulse here. The waveforms calculated by any of the spatial

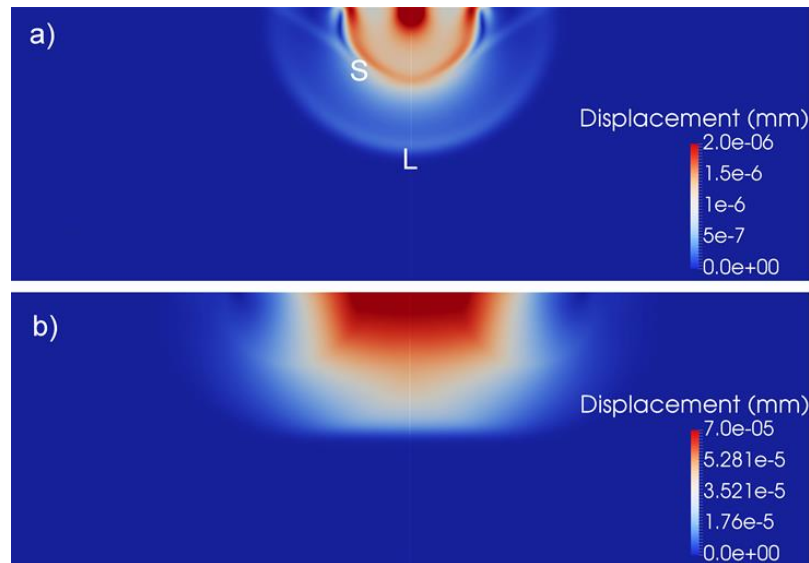


Fig. 5 The shape of the wavefronts 400 ns after irradiation of the surface by the laser beam. The pulse duration is 17 ns and the spot radius is: a) 0.15 mm, and b) 2 mm

distribution Eqs. (11)-(14) differ only by a constant multiplier. Therefore, any one of these four equations can be used for modeling the laser ultrasonics process. In what follows, Eq. (13) will be used for the spatial distribution of the laser pulse.

Laser ultrasonics is modeled in the ablation regime by using laser spots with radii of 0.15, 1, 1.5 and 2 mm to study the effects of spot radius on generation of ultrasonic waves. Fig. 5 shows the wavefronts of the generated waves by laser impulses having spot radii of 0.15 and 2 mm. For the smaller spot radius, the wavefront is approximately spherical (Fig. 5a); however, for the larger spot radius, the wavefront is close to a flat plane (Fig. 5b). As the radius of the laser spot increases, the longitudinal and transverse waves start to broaden and lose their sharpness.

In Fig. 6a, the laser energy density is constant, and the amplitudes of the longitudinal and transverse waves are gradually increased by increasing the radius of the laser spot. In addition, it takes longer for both the longitudinal and transverse waves to reach the bottom surface of the specimen as shown on the normalized graphs of Fig. 6b. As the size of the laser spot increases, the resulting waves become broader, which in turn slightly increases the arrival time of the wave at the bottom of the specimen. The frequency spectra corresponding to signals shown in Fig. 6a are shown in Fig. 6c where it is noted that the frequency spectra have not been much affected by variations of the laser spot radius.

In the next step, the effects of pulse duration on ultrasonic waves is considered. The laser pulse duration is sequentially set to 17, 34, 68 and 136 ns and its effect on the generated ultrasonic waves is examined. By keeping the laser energy density constant and increasing the pulse duration, the amplitudes of both the longitudinal and transverse waves has increased, Fig. 7a. If the curves are normalized (Fig 7b), the echoes become sharper at shorter pulse lengths and as the length of the laser pulse increases, the longitudinal and transverse waves broaden. The frequency spectra of these waves are plotted in Fig. 7c. As shown in Fig. 7c, by changing the pulse length, no significant changes occur in frequency spectrum.

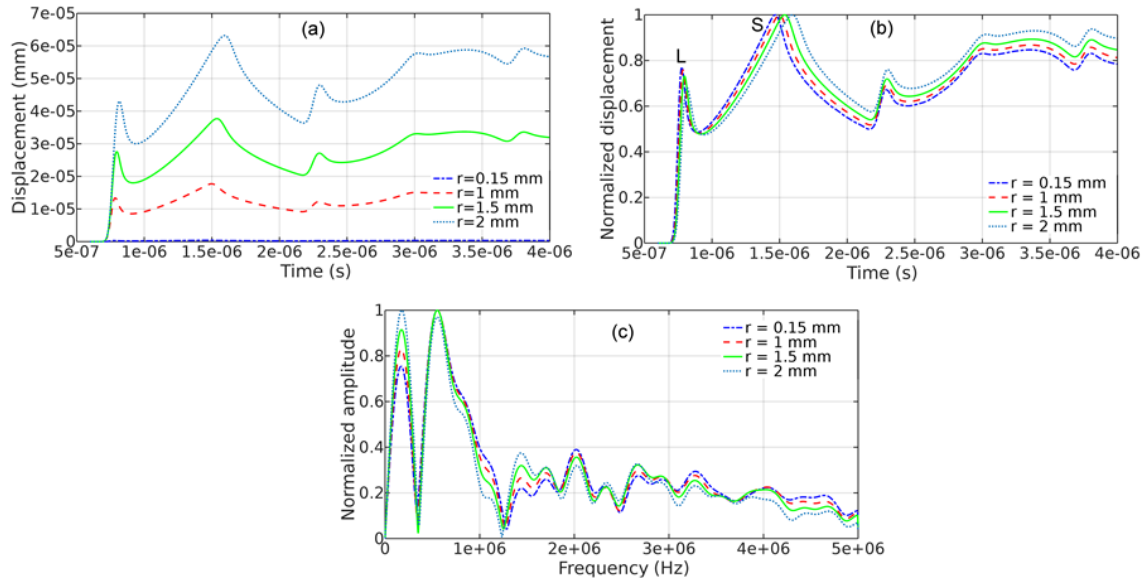


Fig. 6 Ultrasonic waves received at a node on the bottom surface of the specimen along the centerline of the laser beam. The laser pulse duration is 17 ns and the spot radii are 0.15, 1, 1.5 and 2 mm; a) Time domain signal, b) normalized time domain signal, and c) frequency spectrum

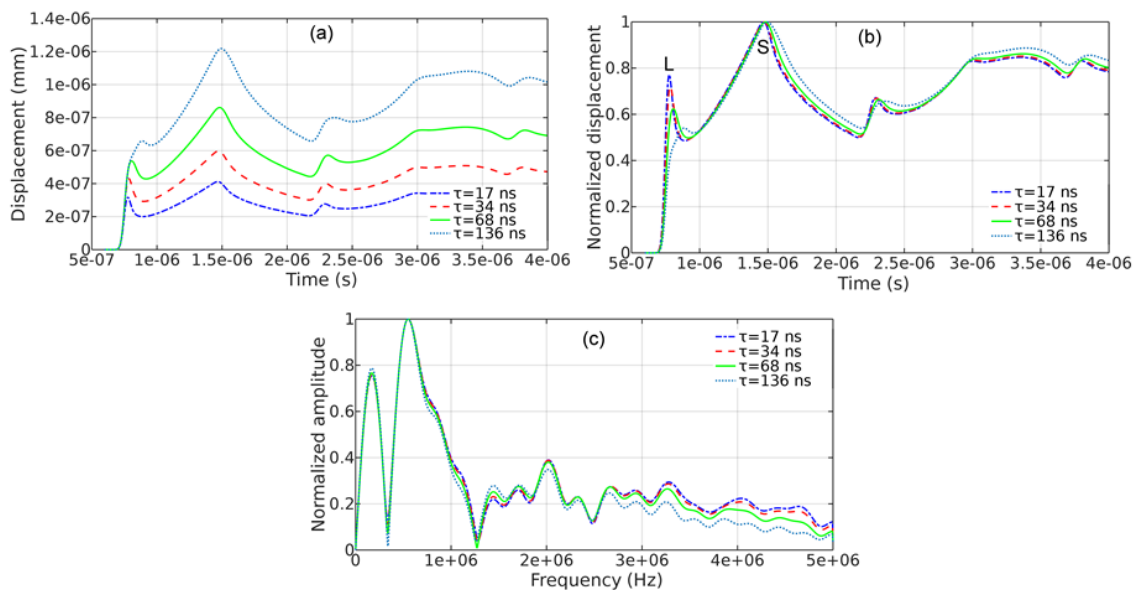


Fig. 7 Ultrasonic waves received at a node on the bottom surface of the specimen. The laser spot radius is 0.15 mm and its pulse durations is 17, 34, 68 and 136 ns. a) time domain signals, b) normalized time domain signals, and c) frequency spectra

Fig. 8 compares the difference of short and long duration laser pulses. In Fig. 8a, the laser pulse has a duration of 17 ns and in Fig. 8b, the pulse duration is 136 ns. Shorter pulse duration has resulted in a sharper wave.

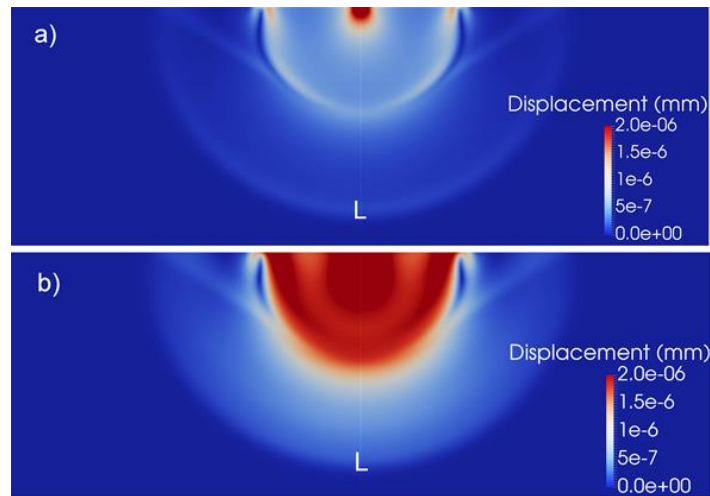


Fig. 8 Ultrasonic waves 660 ns after irradiation of the surface by a laser beam having a spot radius of 0.15 mm and a pulse duration of: a) 17 ns, and b) 136 ns

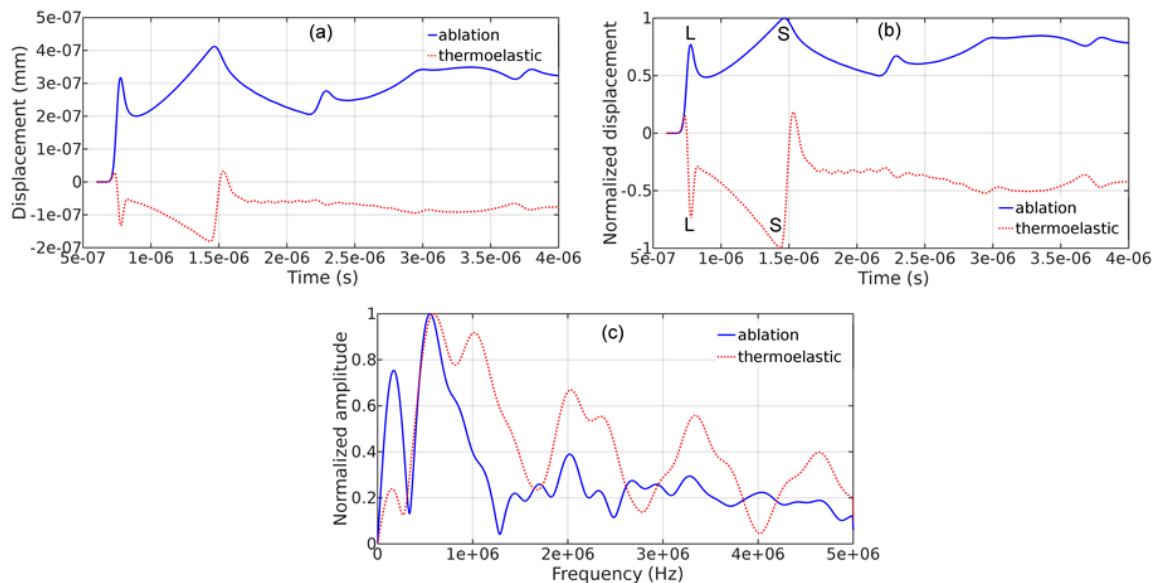


Fig. 9 Ultrasonic waves received from a node on the bottom surface of the specimen along the centerline of the laser beam. The laser spot radius is 0.15 mm, its pulse durations is 17 ns and its energy density is 3.97 J/cm² (for thermoelastic regime) and 78 J/cm² (for ablation regime). a) Time domain signal, b) normalized time domain signal, and c) frequency spectrum

4.2 Comparison of ablation and thermoelastic regimes

When the energy density of the laser is less than the melting and evaporation threshold of the material, the instantaneous thermal expansion of the surface will lead to the formation of an ultrasonic wave inside the specimen. In this case, the test is carried out in thermoelastic regime. When the laser beam hits the surface of an isotropic material, part of the electromagnetic energy of

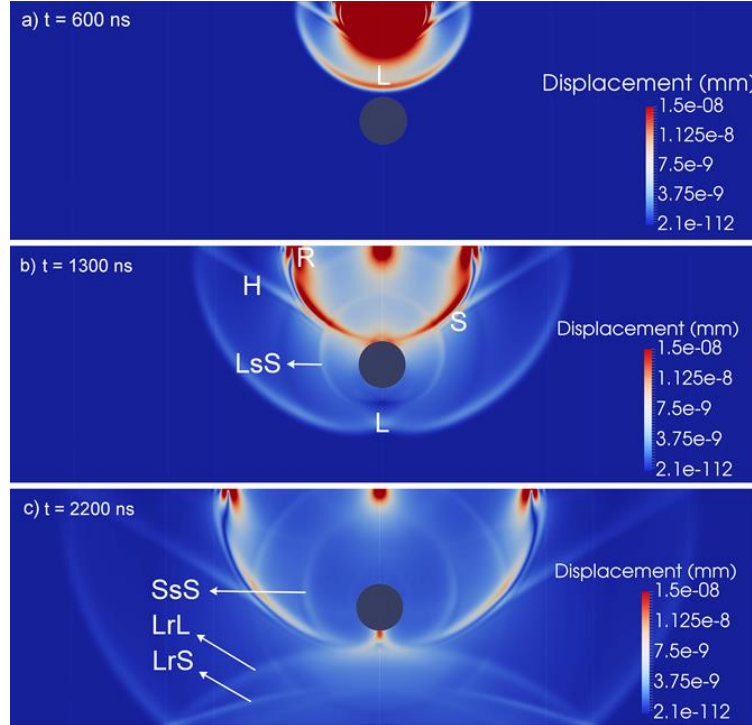


Fig. 10 Ultrasonic wave interaction with a side-drilled hole (SDH) for a laser with an energy of 20 mJ and pulse duration of 6 ns at a) $t=600$ ns b) $t=1300$ ns c) $t=2200$ ns

the laser beam is absorbed by the surface causing the surface to heat up. This heat transfer is expressed by the following equation (Liu *et al.* 2016):

$$\rho C_p \frac{\partial T(x, y, t)}{\partial t} = \nabla(k \nabla T(x, y, t)) + Q \quad (17)$$

where $T(x, y, t)$ is temperature distribution at time t , y axis is along the depth and x axis is along the length of the specimen. C_p , ρ and k are the specific heat capacity, density, and thermal conductivity at constant pressure, respectively, and Q is the energy density of the heat source. Since the laser pulse usually acts as a heat flux instead of a heat source ($Q = 0$), Eq. (17) can be simplified as follows (Liu *et al.* 2016, Zhang *et al.* 2015):

$$\rho C_p \frac{\partial T(x, y, t)}{\partial t} = \frac{\partial}{\partial x} \left(k \frac{\partial T(x, y, t)}{\partial x} \right) + \frac{\partial}{\partial y} \left(k \frac{\partial T(x, y, t)}{\partial y} \right) \quad (18)$$

The boundary conditions are (Liu *et al.* 2016, Zhang *et al.* 2015):

$$-k \frac{\partial T(x, y, t)}{\partial y} \Big|_{y=b} = \frac{E(1-R)f(x)g(t)}{A}, \quad \frac{\partial T(x, y, t)}{\partial y} \Big|_{y=0} = 0 \quad (19)$$

where $f(x)$ and $g(t)$ are the spatial and temporal distributions of the laser beam, respectively. Eq. (14) was used for $f(x)$, and $g(t)$ was calculated from the following equation (Pei *et al.* 2012, Wang *et al.* 2007, Zhang *et al.* 2015, Veres *et al.* 2013):

$$g(t) = 8 \frac{t^3}{\tau^4} \exp\left(\frac{-2t^2}{\tau^2}\right) \quad (20)$$

The coordinate $y = h$ corresponds to the upper surface and $y = 0$ corresponds to the bottom surface of the specimen where h is the specimen thickness. A laser density of 3.97 J/cm^2 is used for generating the ultrasonic wave in the thermoelastic regime. Eqs. (14)-(20) are used to model the spatial and temporal distribution of the laser pulse, respectively. The rest of the parameters are the same as those used for the ablation regime in Section 4.1. The ultrasonic wave is received at the bottom surface of the specimen and the output signal is compared with the results obtained in ablation regime in Fig. 9. In Fig. 9a, the amplitude of the signal resulting from the ablation regime is higher than the signal of the thermoelastic regime. However, in the normalized graphs of the signals, the transverse wave is sharper in thermoelastic regime (Fig. 9b) and the frequency bandwidth is larger (Fig. 9c).

4.3 Defective sample

Ultrasonic testing is widely used for detection and evaluation of defects and characterization of industrial components (Steiner 1992, Jamali *et al.* 2011). In this Section, the proposed equations are used for developing a finite element model for a defective sample. The experimental results for this sample are already available in the literature and therefore, the numerical results can be validated by them. The test specimen is made from aluminum and its thickness is 10 mm. A 1-mm radius side-drilled hole (SDH) is located under the irradiation point at a depth of 5 mm in the specimen. The laser energy and pulse duration are 20 mJ and 6 ns, respectively. A mesh size of 0.03 mm, time increment of 2 ns and adiabatic coefficient of 2.0 are used in this model. The position of the defect (SDFH) and the propagation of ultrasonic waves, as they hit the SDH, are shown in Fig. 10. As shown in Figs. 10a and 10b, by irradiating the laser beam on the surface, longitudinal (L), shear (S), Rayleigh (R) and head (H) waves are simultaneously generated in the specimen. The wavefront of the transverse wave is at an angle of approximately 45 degrees with respect to a horizontal line, and the wavefront of the longitudinal wave is almost vertical. When the longitudinal wave hits the defect, part of it is scattered. The scattered shear wave resulting from mode conversion (LsS) at $t = 1300$ ns is shown in Fig. 10b. The longitudinal wave is reflected after hitting the bottom surface of the specimen (LrL) and part of it is mode converted into a shear wave designated as LrS. After a while, the S-wave also strikes the defect and part of it is scattered (SsS). These waves are shown in Fig. 10c at $t = 2200$ ns.

The time-displacement diagram for a point at the bottom of this specimen and along the laser beam is extracted and compared with the experimental results of Liu *et al.* (2021) in Fig. 11a. The first echo is due to the longitudinal wave (L) and the second echo is the scattered shear wave due to mode conversion (LsS). The third echo comes from the reflection of the S-wave from the SDH after mode conversion (SsL). The fourth echo is the longitudinal wave arriving at the backwall after first reflecting from the backwall and then reflecting from the defect (LrLrL). The wave that reaches the bottom surface of the sample at $t = 3258$ ns (fifth echo) is due to the shear wave (S). The frequency spectra corresponding to Fig. 11a are shown in Fig. 11b. Figs. 11c and 11d show the time-displacement plots and their frequency spectra for an intact sample (no defect). Good agreement between numerical and experimental results confirms the validity of the developed model. Possible reasons for slight differences in numerical and experimental results were already discussed in Section 4.1.

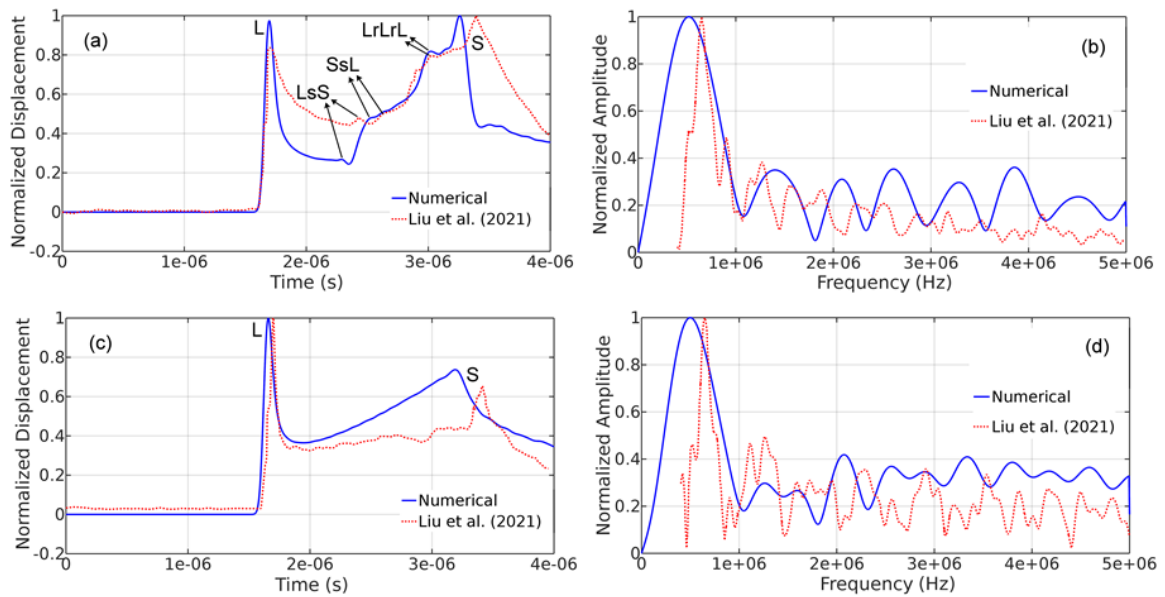


Fig. 11 Ultrasonic waves received at a node on the bottom surface of the sample along the centerline of the laser beam. The laser has an energy of 20 mJ and pulse duration of 6 ns. a) Time-domain signals of the defective specimen, b) frequency spectra of (a), c) time-domain signals of the intact specimen, and d) frequency spectra of (c)

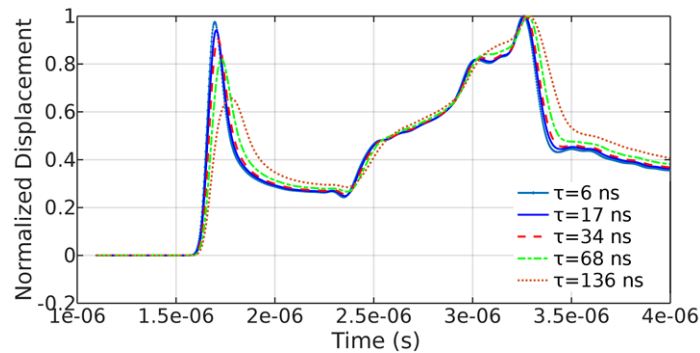


Fig. 12 Time-domain signal for a node on the bottom surface of the specimen along the laser beam. The laser has an energy of 20 mJ and pulse durations of 6, 17, 34, 68 and 136 ns

The defective specimen was modeled with pulse durations of 6, 17, 34, 68, and 136 ns, and the displacements were measured at a node on the bottom surface of the specimen along the laser beam. As shown in Fig. 12, with increase in pulse duration, the longitudinal wave gradually broadens and LsS and LrLrL waves fade out.

5. Conclusions

While the finite element modeling of LU in thermoelastic regime has been widely studied, the LU in ablation regime has not received much attention.

- In this paper, various equations used for the spatial and temporal distribution of the pressure pulse in finite element modeling in two different laser applications, i.e., laser ultrasonics and laser shock peening, were examined and the best combination of these equations for modeling the LU process in ablation regime was identified. It was noticed that the available spatial distribution equations do not differ much from one another, but the choice of the temporal distribution equation is very important.

- By using the new model, the effects of laser spot radius and laser pulse duration on the amplitude, shape and frequency spectrum of ultrasonic waves were studied.

- By keeping the energy density constant and increasing the spot radius, the amplitude of all waves increased. Furthermore, increase of the spot radius led to the increase of the travel times of both the longitudinal and transverse waves.

- Keeping the energy density constant and increasing the pulse duration also resulted in the increase of the amplitudes of both longitudinal and transverse waves.

- The interaction of LU waves with a side-drilled hole (representing a defect) was also investigated. The LU in ablation regime was also compared with LU in thermoelastic regime and the results were consistent with the physics of these two types of tests.

- It can be concluded that the proposed model is accurate and can be used for finite element modeling of the LU process in ablation regime.

References

- Abbas, S.H. and Lee, J.R. (2018), "High-speed angular-scan pulse-echo ultrasonic propagation imager for in situ non-destructive evaluation", *Adv. Comput. Des.*, **22**(2), 223-230.
<https://doi.org/10.12989/sss.2018.22.2.223>.
- Achinta, M. and Nowell, D. (2011), "Eigenstrain modelling of residual stresses generated by laser shock peening", *J. Mater. Process. Technol.*, **211**, 1091-1101.
<https://doi.org/10.1016/j.jmatprotec.2011.01.011>.
- Arrigoni, M., Hu, Q., Boustie, M., Berthe, L. and Monchalain, P. (2008), "B-scan simulations with Abaqus for laser ultrasonic inspection of structures", *Proceedings of the 1st International Symposium on Laser Ultrasonics: Science, Technology and Applications*, Montreal, Canada, July 16-18.
- ASTER (2017), *Code-Aster User Manual, version 13.4, Analysis of Structures and Thermomechanics for Studies and Research*, Electricite De France R&D Department; Paris, France.
- Avillez, M.A., Anela, G.J. and Breitschwerdt, D. (2018), "Variability of the adiabatic parameter in monoatomic thermal and non-thermal plasmas", *Astron. Astrophys.*, **616**, A58.
<https://doi.org/10.1051/0004-6361/201832948>.
- Cavuto, A., Martarelli, M., Pandarese, G., Revel, G.M. and Tomasini, E.P. (2015), "Experimental investigation by laser ultrasonics for high speed train axle diagnostics", *Ultrason.*, **55**, 48-57.
<https://doi.org/10.1016/j.ultras.2014.08.010>.
- Choi, S. and Jhang, K.Y. (2018), "Internal defect detection using laser-generated longitudinal waves in ablation regime", *J. Mech. Sci. Technol.*, **32**(9), 4191-4200. <https://doi.org/10.1007/s12206-018-0817-1>.
- Dai, Y., Xu, B.Q., Luo, Y., Li, H. and Xu, G.D. (2010), "Finite element modeling of interaction of laser-generated ultrasound with a surface-breaking notch in an elastic plate", *Opt. Laser Technol.*, **42**, 693-697.
<https://doi.org/10.1016/j.optlastec.2009.11.012>.
- Davies, S.J., Edwards, C., Taylor, G.S. and Palmer, B.P. (1993), "Laser-generated ultrasound: its properties, mechanisms and multifarious applications", *J. Phys. D: Appl. Phys.*, **26**(3), 329-348.
<https://doi.org/10.1088/0022-3727/26/3/001>.
- Deiterding, R., Cirak, F., Mauch, S.P. and Meiron, D.I. (2007), "A virtual test facility for simulating

- detonation and shock-induced deformation and fracture of thin flexible shells”, *Int. J. Multisc. Comput. Eng.*, **6**(1), 47-63. https://doi.org/10.1007/11758525_17.
- Ecault, R., Touchard, F., Boustie, M., Berthe, L. and Dominguez, N. (2016), “Numerical modeling of laser-induced shock experiments for the development of the adhesion test for bonded composite materials”, *Compos. Struct.*, **152**, 382-394. <https://doi.org/10.1016/j.compstruct.2016.05.032>.
- Fassbender, S., Hoffmann, B. and Arnold, W. (1989), “Efficient generation of acoustic pressure waves by short laser pulses”, *Mater. Sci. Eng.*, **A122**, 37-41. [https://doi.org/10.1016/0921-5093\(89\)90768-5](https://doi.org/10.1016/0921-5093(89)90768-5).
- Gondrad, C., Nadal, M.H. and Hermerel, C. (1998), “Three ultrasonic devices for the elastic moduli determination at high temperatures”, *Rev. Prog. Quant. Nondestr. Eval.*, **17**, 867-874. https://doi.org/10.1007/978-1-4615-5339-7_112.
- Guo, Y., Yang, D., Chang, Y. and Gao, W. (2014), “effect of oblique force source induced by laser ablation on ultrasonic generation”, *Opt. Express*, **22**(1), 166-176. <https://doi.org/10.1364/OE.22.000166>.
- Halilovic, M., Issa, S., wallin, M., Hallberg, H. and Ristinmaa, M. (2016), “Prediction of the residual state in 304 austenitic steel after laser shock peening - Effects of plastic deformation and martensitic phase transformation”, *Int. J. Mech. Sci.*, **111-112**, 24-34. <https://doi.org/10.1016/j.ijmecsci.2016.03.022>.
- Hfaiedh, N., Peyre, P., Song, H., Popa, I., Ji, V. and Vignal, V. (2015), “Finite element analysis of laser shock peening of 2050-T8 aluminum alloy”, *Int. J. Fatigue*, **70**, 480-489. <https://doi.org/10.1016/j.ijfatigue.2014.05.015>.
- Hopko, S.N. and Ume, I.C. (1999), “Laser ultrasonics: simultaneous Generation by means of thermoelastic expansion and material ablation”, *J. Nondestr. Eval.*, **18**(3), 91-98. <https://doi.org/10.1023/A:1021856526734>.
- Jamali, J., Naei, M.H., Honarvar, F. and Rajabi, M. (2011), “Acoustic scattering and radiation force function experienced by functionally graded cylindrical shells”, *J. Mech.*, **27**(2), 227-243. <https://doi.org/10.1017/jmech.2011.27>.
- Kim, J.H., Kim, Y.J. and Kim, J.S. (2013), “Effects of simulation parameters on residual stresses for laser shock peening finite element analysis”, *J. Mech. Sci. Technol.*, **27**(7), 2025-2034. <https://doi.org/10.1007/s12206-012-1263-0>.
- Lee, S.E., Liu, P., Ko, Y.W., Sohn, H., Park, B. and Hong, J.W. (2019), “Study on effect of laser-induced ablation for Lamb waves in a thin plate”, *Ultrason.*, **91**, 121-128. <https://doi.org/10.1016/j.ultras.2018.07.019>.
- Liu, P., Jang, J. and Sohn, H. (2020), “Crack localization by laser-induced narrowband ultrasound and nonlinear ultrasonic modulation”, *Adv. Comput. Des.*, **25**(3), 301-310. <https://doi.org/10.12989/sss.2020.25.3.301>.
- Liu, P., Nazirah, A.W. and Sohn, H. (2016), “Numerical simulation of damage detection using laser-generated ultrasound”, *Ultrason.*, **69**, 248-258. <https://doi.org/10.1016/j.ultras.2016.03.013>.
- Liu, W.B., Yan, W.B., Liu, H., Tong, C.G., Fan, Y.X. and Tao, Z.Y. (2021), “Internal cylinder Identification based on different transmission of longitudinal and shear ultrasonic waves”, *Sens.*, **21**, 723. <https://doi.org/10.3390/s21030723>.
- Ma, Y., Hu, Z., Tang, Y., Ma, S., Chu, Y., Li, X., Luo, W., Guo, L., Zeng, X. and Lu, Y. (2020), “Laser opto-ultrasonic dual detection for simultaneous compositional, structural, and stress analyses for wire + arc additive manufacturing”, *Addit. Manuf.*, **31**, 100956. <https://doi.org/10.1016/j.addma.2019.100956>.
- Martynenko, A.S., Skobelev, I.Y. and Pikuz, S.A. (2019), “Possibility of estimating high-intensity-laser plasma parameters by modelling spectral line profiles in spatially and time-integrated X-ray emission”, *Appl. Phys. B*, **125**, 31. <https://doi.org/10.1007/s00340-019-7149-4>.
- Mi, B. and Ume, I.C. (2002), “Parametric studies of laser generated ultrasonic signals in ablative regime: time and frequency domains”, *J. Nondestr. Eval.*, **21**(1), 23-33. <https://doi.org/10.1023/A:1019980725994>.
- Murray, T.W. and Wanger, J.W. (1998), “Thermoelastic and ablative generation of ultrasound: source effects”, *Rev. Prog. Quant. Nondestr. Eval.*, **17**, 619-625. https://doi.org/10.1007/978-1-4615-5339-7_80.
- Pan, Y., Chigarev, N. and Audoin, B. (2010), “Bulk waves excited by a laser line pulse in a bi-layer cylinder”, *J. Phys. Conf. Ser.*, **214**, 012044. <https://doi.org/10.1088/1742-6596/214/1/012044>.

- Pan, Y., Rossignol, C. and Audoin, B. (2004), "Acoustic waves generated by a laser line pulse in cylinders; Application to the elastic constants measurement", *J. Acoust. Soc. Am.*, **115**(4), 1537-1545.
<https://doi.org/10.1121/1.1651191>.
- Pei, C., Demachi, K., Zhu, H., Fukuchi, T., Koyama, K. and Uesaka, M. (2012), "Inspection of Cracks Using Laser-Induced Ultrasound with Shadow Method: Modeling and Validation", *Opt. Laser Technol.*, **44**, 860-865. <https://doi.org/10.1016/j.optlastec.2011.11.018>.
- Rao, Z., Liu, J., Wang, P.C., Li, Y. and Liao, S. (2014), "Modeling of cold metal transfer spot welding of AA6061-T6 Aluminum alloy and Galvanized mild Steel", *J. Manuf. Sci. Eng.*, **136**(5), 051001.
<https://doi.org/10.1115/1.4027673>.
- Sakamoto, J.M.S., Tittmann, B.R., Baba, A. and Pacheco, G.M. (2011), "Directivity measurements in aluminum using a laser ultrasonics system", *J. Phys. Conf. Ser.*, **278**, 012032.
<https://doi.org/10.1088/1742-6596/278/1/012032>.
- Sherman, B., Liou, H.C. and Balogun, O. (2015), "Thin film interface stresses produced by high amplitude laser generated surface acoustic waves", *J. Appl. Phys.*, **118**, 135303. <https://doi.org/10.1063/1.4931937>.
- Steiner, K.V. (1992), *Defect Classifications in Composites Using Ultrasonic Nondestructive Evaluation Techniques*, In *Damage Detection in Composite Materials.*, ASTM International.
- Stratoudaki, T., Edwards, C., Dixon, S. and Palmer, S.B. (2003), "Optical absorption of epoxy resin and its role in the laser ultrasonic generation mechanism in composite materials", *Rev. Quant. Nondestr. Eval.*, **22**, 965-972. <https://doi.org/10.1063/1.1570238>.
- Taheri, H., Koester, L.W., Bigelow, T.A. and Bond, L.J. (2017), "Thermoelastic finite element modeling of laser generated ultrasound in additive manufacturing materials", *Proceedings of the ASNT Annual Conference*, 188-198.
- Veres, I.A., Berer, T. and Burgholzer, P. (2013), "Numerical modeling of thermoelastic generation of ultrasound by laser irradiation in the coupled thermoelasticity", *Ultrason.*, **53**, 141-149.
<https://doi.org/10.1016/j.ultras.2012.05.001>.
- Wang, C., Wang, X., Xu, Y. and Gao, Z. (2016), "Numerical modeling of the confined laser shock peening of the OFHC copper", *Int. J. Mech. Sci.*, **108-109**, 104-114.
<https://doi.org/10.1016/j.ijmecsci.2016.02.002>.
- Wang, J., Shen, Z., Xu, B., Ni, X., Guan, J. and Lu, J. (2007), "Numerical simulation of laser-generated ultrasound in non-metallic material by the finite element method", *Opt. Laser Technol.*, **39**, 806-813.
<https://doi.org/10.1016/j.optlastec.2006.01.009>.
- Yang, J., Liu, P., Yang, S., Lee, H. and Sohn, H. (2015), "Laser based impedance measurement for pipe corrosion and bolt-loosening detection", *Smart Struct. Syst.*, **15**(1), 41-55.
<https://doi.org/10.12989/sss.2015.15.1.041>.
- Zhang, K., Zhou, Z., Zhou, J. and Sun, G. (2015), "Characteristics of laser ultrasound interaction with multi-layered dissimilar metals adhesive interface by numerical simulation", *Appl. Surf. Sci.*, **353**, 284-290.
<https://doi.org/10.1016/j.apsusc.2015.06.103>.
- Zhao, J., Dong, Y. and Ye, C. (2017), "Laser shock peening induced residual stresses and the effect on crack propagation behavior", *Int. J. Fatigue*, **100**, 407-417. <https://doi.org/10.1016/j.ijfatigue.2017.04.002>.
- Zhao, Y., Shen, Z., Lu, J. and Ni, X. (2007), "A finite element model for laser-induced leaky waves at fluid-solid interfaces", *Phys. Lett. A*, **370**, 104-109. <https://doi.org/10.1016/j.physleta.2007.05.071>.
- Zhou, Z., Zhang, K., Zhou, J., Sun, G. and Wang, J. (2015), "Application of laser ultrasonic technique for non-contact detection of structural surface-breaking cracks", *Opt. Laser Technol.*, **73**, 173-178.
<https://doi.org/10.1016/j.optlastec.2015.04.026>.